coatings

MDPI

Article

Powder Synthesized from Aqueous Solution of Calcium Nitrate and Mixed-Anionic Solution of Orthophosphate and Silicate Anions for Bioceramics Production

Daniil Golubchikov [1,*], Tatiana V. Safronova [1,2,*], Elizaveta Nemygina [1], Tatiana B. Shatalova [1,2], Irina N. Tikhomirova [3], Ilya V. Roslyakov [1,4], Dinara Khayrutdinova [5], Vadim Platonov [2], Olga Boytsova [2], Maksim Kaimonov [1], Denis A. Firsov [2] and Konstantin A. Lyssenko [2]

1 Department of Materials Science, Lomonosov Moscow State University, Building, 73, Leninskie Gory, 1, 119991 Moscow, Russia
2 Department of Chemistry, Lomonosov Moscow State University, Building, 3, Leninskie Gory, 1, 119991 Moscow, Russia
3 Department of General Technology of Silicates, Mendeleev University of Chemical Technology, Building, 1, Geroyev Panfilovtsev, 20, 125480 Moscow, Russia
4 Kurnakov Institute of General and Inorganic Chemistry, Russian Academy of Sciences, Leninskii Prosp., 31, 119071 Moscow, Russia
5 A.A. Baikov Institute of Metallurgy and Materials Science, Russian Academy of Sciences, Leninskii Prosp., 49, 119334 Moscow, Russia
* Correspondence: golubchikovdo@my.msu.ru or dddannn2113@gmail.com (D.G.); safronovatv@my.msu.ru (T.V.S.)

Abstract: Synthesis from mixed-anionic aqueous solutions is a novel approach to obtain active powders for bioceramics production in the CaO-SiO_2-P_2O_5-Na_2O system. In this work, powders were prepared using precipitation from aqueous solutions of the following precursors: $Ca(NO_3)_2$ and Na_2HPO_4 (CaP); $Ca(NO_3)_2$ and Na_2SiO_3 (CaSi); and $Ca(NO_3)_2$, Na_2HPO_4 and Na_2SiO_3 (CaPSi). Phase composition of the CaP powder included brushite $CaHPO_4{\cdot}2H_2O$ and the CaSi powder included calcium silicate hydrate. Phase composition of the CaPSi powder consisted of the amorphous phase (presumably containing hydrated quasi-amorphous calcium phosphate and calcium silicate phase). All synthesized powders contained $NaNO_3$ as a by-product. The total weight loss after heating up to 1000 °C for the CaP sample—28.3%, for the CaSi sample—38.8% and for the CaPSi sample was 29%. Phase composition of the ceramic samples after the heat treatment at 1000 °C based on the CaP powder contained β-$NaCaPO_4$ and β-$Ca_2P_2O_7$, the ceramic samples based on the CaSi powder contained α-$CaSiO_3$ and $Na_2Ca_2Si_2O_7$, while the ceramics obtained from the CaPSi powder contained sodium rhenanite β-$NaCaPO_4$, wollastonite α-$CaSiO_3$ and $Na_3Ca_6(PO_4)_5$. The densest ceramic sample was obtained in CaO-SiO_2-P_2O_5-Na_2O system at 900 °C from the CaP powder (ρ = 2.53 g/cm^3), while the other samples had densities of 0.93 g/cm^3 (CaSi) and 1.22 (CaPSi) at the same temperature. The ceramics prepared in this system contain biocompatible and bioresorbable phases, and can be recommended for use in medicine for bone-defect treatment.

Keywords: mixed-anionic solution; precipitation; brushite; calcium silicate hydrate; amorphous calcium phosphate; sodium nitrate; calcium pyrophosphate; sodium rhenanite; sodium-calcium silicate; wollastonite; bioceramics

check for updates

Citation: Golubchikov, D.; Safronova, T.V.; Nemygina, E.; Shatalova, T.B.; Tikhomirova, I.N.; Roslyakov, I.V.; Khayrutdinova, D.; Platonov, V.; Boytsova, O.; Kaimonov, M.; et al. Powder Synthesized from Aqueous Solution of Calcium Nitrate and Mixed-Anionic Solution of Orthophosphate and Silicate Anions for Bioceramics Production. *Coatings* **2023**, *13*, 374. https://doi.org/10.3390/coatings13020374

Academic Editor: Richard Drevet

Received: 31 December 2022
Revised: 1 February 2023
Accepted: 2 February 2023
Published: 7 February 2023

1. Introduction

Modern science faces a problem of increasing levels of bone diseases, traumas and cancers. Thereby, the development of bone repair orthopedic approaches as well as enhancement of implemented biomaterials is crucial [1,2]. Bone tissues possess a great regenerative potential and suitable biomaterials are required to support natural regeneration process [3–6]. One of the crucial processes of native bone forming is angiogenesis [7],

which is vital for bone healing [8]. The most commonly used biomaterials in the field of bone tissue engineering are polymers [9–11], composites [12], as well as glass and ceramics, obtained in systems containing calcium phosphates and silicates [13–16]. Such materials are also required to provide a sufficient mechanical support and appropriate environment for cell attachment, proliferation, and differentiation [17,18].

Among the first steps in this area were materials in the Na_2O-CaO-SiO_2-P_2O_5 system, suggested by L. L. Hench [19]. This study marked the beginning of calcium-sodium phosphate-silicate glass-ceramics development as well as application of such materials in bone implant production. L.L. Hench et al. [20] demonstrated that synthesized surface-active bioglass-ceramics can be used in vivo without inflammation.

Materials synthesized in the considered system tend to be osteoinductive, since the presence of Si-containing ions is suggested to stimulate the proliferation of human aortic endothelial cells as well as to support the expression of genes encoding the proangiogenic downstream cytokines [21], which is necessary for successful angiogenesis processes [22].

A special part of the Na_2O-CaO-SiO_2-P_2O_5 system is the CaO-SiO_2 system, in which two congruently melting compounds, Ca_2SiO_4 and $CaSiO_3$ (wollastonite), and two incongruently melting compounds, Ca_3SiO_5 (stable from 1250 to 2050 °C), and $Ca_3Si_2O_7$ (stable from low temperature to 1464 °C), can be obtained [23]. Congruently melting compounds are more promising for bone tissue engineering: for example, 3D-printed β-Ca_2SiO_4 scaffolds sintered at a higher temperature stimulated the adhesion, proliferation, ALP activity, and osteogenic-related gene expression of rBMSCs [24]. $CaSiO_3$ ceramics have been extensively researched as biomaterial to replace other materials due to their superior biological activity, for example, compared to hydroxyapatite (HA) [25] showing their potential prospects in in vivo trials [26]. In addition, calcium silicate ceramics can be used for skin healing and cartage regeneration [27]. In [28], silicate ceramics are obtained by solid-phase synthesis from a mixture of powders.

In the CaO-P_2O_5, which is a part of the Na_2O-CaO-SiO_2-P_2O_5 system, the following biocompatible and bioresorbable phases of tricalcium phosphate ($Ca_3(PO_4)_2$) and calcium pyrophosphate ($Ca_2P_2O_7$) [29] can be obtained.

In Na_2O-CaO-P_2O_5 sodium-substituted tricalcium phosphate $Ca_{10}Na(PO_4)_7$, sodium rhenanite β-$NaCaPO_4$, mixed sodium-calcium pyrophosphate ($CaNa_2P_2O_7$) [29] and mixed sodium-calcium phosphate ($Na_3Ca_6(PO_4)_5$) can be obtained.

In the CaO-SiO_2-P_2O_5, as a part of the Na_2O-CaO-SiO_2-P_2O_5 system, two main phases can be obtained: silicocarnotite ($Ca_5(PO_4)_2SiO_4$), with a structure type carnotite and a wide range of solid solutions [30,31], and nagelshmidtite ($Ca_7Si_2P_2O_{16}$) [32]. Both phases provide satisfactory biocompatibility. The addition of sodium to this system leads to the appearance of $Na_2Ca_2Si_3O_9$ and $Na_2CaSi_3O_8$ after the sintering of material above 600 °C [33].

There are several approaches for obtaining ceramics or glass-ceramics in the CaO-SiO_2-P_2O_5-Na_2O system. First of all, the samples can be obtained in the form of glasses with subsequent crystallization during the heat treatment at an appropriate temperature [34]; nevertheless, this method has final phase composition limitations. In this case, the bioactive glass decomposition occurs, which leads to the appearance of additional crystalline phases. The composition of this phases directly depends on the composition of the initial mixture. For example, using the mixture of the initial components with the ratio of SiO_2:NaO_2:CaO = 41.8:26.7:31.5 (mol) makes it possible to obtain the $Na_2Ca_2Si_2O_7$ phase [35]. This phase was also synthesized in [36] from the mixture of reagent grade Na_2CO_3, CaO, bovine bone (P_2O_5 source), and rice husk (SiO_2 source), as additional to the $Na_6Ca_3Si_6O_{18}$ main phase. Nevertheless, the sample containing this phase showed good results in mechanical properties and in in vitro tests.

Another approach to obtain ceramics in the considered CaO-SiO_2-P_2O_5-Na_2O system is based on the use of hydroxyapatite or tricalcium phosphate powders as a filler and an aqueous solution of sodium silicate as a binder [37]. This method leads to the formation of two main phases, which are β-rhenanite (β-$NaCaPO_4$) and sodium calcium phosphate

($Na_3Ca_6(PO_4)_5$) after heat treatment. These phases are biocompatible and are used for the restoration of bone-tissue defects [38,39].

It is also possible to prepare ceramic materials using intermediate phases precipitated from the solution (such as hydroxyapatite and amorphous sodium silicate), which can be converted into final phases (sodium rhenanite, calcium-sodium silicate, and wollastonite) during the heat treatment process [37,40].

In addition, it is possible to print scaffolds from a composite of calcium phosphate powders and 45S5 Bioglass using a cementation reaction during printing [41,42]. In [42], calcium hydrogen phosphate dihydrate ($CaHPO_4 \cdot 2H_2O$) was formed as a result of the cementing reaction. And the final phase composition of material after the heat treatment at 1000 °C contained sodium rhenanite ($NaCaPO_4$) and wollastonite ($CaSiO_3$).

Ceramics in the CaO-SiO_2-P_2O_5-Na_2O system can be obtained from powders synthesized from solutions. To obtain such ceramics, active powders with a highly homogeneous distribution of components are required. Amorphous powders synthesized from mixed-anionic solutions have the necessary homogeneity.

There are some examples of powders synthesized from mix-anionic HPO_4/P_2O_7 [43] P_2O_7/CO_3 [44], HPO_4/CO_3 [45,46], or mix-cationic K/Na [47] aqueous solutions with appropriate homogeneity that were used for the ceramic materials preparation. Preservation of reaction by-product as a component of the powder mixture also can be used as a method of preparation of powder mixtures with high homogeneity [25,48,49].

However, an approach involving synthesis from mixed-anionic solutions is more interesting, since this method leads to a more homogeneous distribution of components in the powder mixture [43–46]. In addition, a chemical approach to the synthesis of mixed-anionic powders makes it possible to obtain more dispersed powders with a larger specific surface area, which are more active, and the sintering process is more effective [48,49]. Additionally, the by-product of the synthesis from mixed-anionic solutions can be kept in the composition to form melts and promote the formation of new phases [48,49]. Thereby, this method can be the most promising approach to obtain ceramics in the CaO-SiO_2-P_2O_5-Na_2O system.

Thus, the aim of the present work consisted in the synthesis of powder, which contains precursors of calcium phosphate and silicate high-temperature phases, as well as the reaction by-product from the mixed-anionic solution, for preparation of composite ceramics in Na_2O-CaO-SiO_2-P_2O_5 system. The obtained powder mixture was implemented as a powder precursor with homogeneous distribution of the components for production of the composite material, while the by-product of synthesis was used both as a participant of the heterogeneous reactions and as a sintering aid.

2. Materials and Methods

2.1. Materials

Powders of calcium nitrate tetrahydrate $Ca(NO_3)_2 \cdot 4H_2O$ (CAS no. 13477-34-4, ACS reagent, Sigma-Aldrich, Mumbai, India), sodium metasilicate pentahydrate $Na_2SiO_3 \cdot 5H_2O$ (CAS no. 10213-79-3, RusKhim, Moscow, Russia), and sodium phosphate dibasic (CAS no. 7558-79-4, BioXtra, Sigma-Aldrich, Gillingham, UK) were used for powder mixture preparation.

2.2. Synthesis of Powders

The synthesis of powders was carried out using the Na_2SiO_3, $Ca(NO_3)_2$, Na_2HPO_4 (Table 1) according to the equations:

$$Ca(NO_3)_2 + Na_2HPO_4 + 2H_2O \rightarrow CaHPO_4 \cdot 2H_2O + 2\ NaNO_3 \quad (1)$$

$$2\ Ca(NO_3)_2 + Na_2HPO_4 + Na_2SiO_3 + xH_2O \rightarrow CaHPO_4 \cdot 2H_2O + CaSiO_3 \cdot xH_2O + 4\ NaNO_3 \quad (2)$$

$$Ca(NO_3)_2 + Na_2SiO_3 + xH_2O \rightarrow CaSiO_3 \cdot xH_2O + 2\ NaNO_3 \quad (3)$$

Table 1. Conditions used for the syntheses of powders from aqueous solutions Na_2SiO_3, Na_2HPO_4, and $Ca(NO_3)_2$.

No.	Labeling	Concentration × Volume		
		Na_2SiO_3	Na_2HPO_4	$Ca(NO_3)_2$
1	CaP	-	0.5 M × 0.5 L	0.5 M × 0.5 L
2	CaPSi	0.5 M × 0.25 L	0.5 M × 0.25 L	0.5 M × 0.5 L
3	CaSi	0.5 M × 0.5 L	-	0.5 M × 0.5 L

The starting salts were dissolved in distilled water at a concentration of 0.5 M, then the calcium salt solution was slowly added to the sodium salt solution in the volume ratios corresponding to the reactions (1–3), and the suspension was stirred for 1 h. The synthesis was carried out at a temperature of 37 °C. Then, the precipitate was filtered using a vacuum filter and evenly distributed over a large surface area and left to dry for 1 week.

Further, the obtained powders were disaggregated in acetone medium using a planetary ball mill (Fritch Pulverisette, Bavaria, Germany) for 10 min in zirconia containers with grinding ZrO_2-media (m_{powder}:m_{balls} = 1:5). After that, when the acetone was completely removed each of the powders was sieved through a polyester sieve with a mesh size of 200 μm.

2.3. Preparation of Ceramic Samples

The obtained samples were pressed into the form of simple disks by uniaxial one-sided pressing on a manual press (Carver Laboratory Press model C, Fred S. Carver, Inc., Wabash, IN, USA) using steel die with a diameter of 12 mm. Pressing was carried out at a pressure of 100 MPa for 10 s.

The pressed samples in the form of disks were fired at 800, 900 and 1000 °C. Additionally, the powders were fired at 400 and 600 °C to control the phase transformations. Heating in the furnace was carried out at a speed of 5 °C/min. The holding time at these temperatures was 2 h. The heat treatment of the samples was carried out in order to study the effect of high temperatures on the initial composition, as well as to determine the mass losses and determine the thermal behavior of the materials in the temperature range mentioned. The linear shrinkage and density of the samples after the heat treatment were also calculated.

2.4. Methods of Analysis

The linear shrinkage after the heat treatment and the density of the samples before and after the heat treatment were calculated using Equations (4) and (5), respectively.

$$\Delta D_{rel} = (D_0 - D)/D_0 \times 100, \%, \quad (4)$$

where:

ΔD_{rel}—linear shrinkage of the sample after the heat treatment, %;

D—diameter of the sample after the heat treatment, cm;

D_0—diameter of the sample after pressing, cm.

$$\rho = m/(h \times \pi D^2/4), g/cm^3, \quad (5)$$

where:

ρ—density of the sample, g/cm^3;

m—weight of the sample, g;

h—thickness of the sample, cm;

D—diameter of the sample, cm.

The mass and the linear dimensions of the samples were measured with accuracy of ±0.001 g and ±0.01 mm, respectively, before and after the heat treatment.

Thermal analysis (TA) including thermogrvimetry (TG) and differential thermal analysis (DTA) was performed using an STA 409 PC Luxx thermal analyzer (NETZSCH, Selb, Germany) during heating in air (10 °C/min, 40–1000 °C), the specimen mass being at least 10 mg. The gas-phase composition was monitored by a Netzsch QMS 403C Aëolos quadrupole mass spectrometer (NETZSCH, Selb, Germany) coupled with a Netzsch STA 409 PC Luxx thermal analyzer (NETZSCH, Selb, Germany). The mass spectra were registered for the following m/Z values: 18 (H_2O); 30 (NO).

The phase composition of the powders obtained after the synthesis was determined by X-ray powder diffraction (XRD) analysis using Rigaku D/Max-2500 diffractometer (Rigaku Corporation, Tokyo, Japan) with a rotating anode (Cu–Ka radiation), angle interval 2Θ: from 2° to 70° (step 2Θ − 0.02°). XRD analysis of the ceramic composition was also implemented using a Rigaku Miniflex 600 diffractometer (CuKα radiation, Kβ filter, and D/teX Ultra detector) in Bragg–Brentano geometry (Rigaku Corporation, Tokyo, Japan) with an angle interval 2Θ from 3° to 70° (step 2Θ − 0.02°). Phase analysis was performed using the ICDD PDF2 database and Match software (version https://www.crystalimpact.com/, 25 December 2022).

Scanning electron microscopy (SEM) images of the synthesized powder and powder mixtures were characterized by SEM on an NVision 40 microscope (Carl Zeiss, Jena, Germany), and SEM images of ceramic samples were taken with Tescan Vega II (Tescan, Brno, Czech Republic) at accelerating voltages from 1 to 20 kV in secondary electron imaging mode (SE2 detector). A chromium/gold layers (≤10 nm in thickness) on the surface of the ceramic sample was applied to the samples (Quorum Technologies spraying plant, Q150T ES, Great Britain, London, UK).

3. Results and Discussion

Table 2 shows weights of the prepared powders after synthesis and drying, weights of by-products calculated from the reactions (1–3) and weights of by-products isolated from the mother liquor by drying. The mass of prepared powders (column 3, Table 2) may include the mass of target minerals and the mass of by-product. In the row of powders CaP, CaPSi, CaSi the weight of the by-product collected from the mother liquor became lower. It was the lowest for CaSi, therefore, the amount of the by-product adsorbed and occluded by powder was the largest. The mass of adsorbed and occluded by-products increases from CaP to CaSi powder. The amount of the isolated reaction by-product apparently can be interpreted as an indirect confirmation of the presence of the largest active surface for CaSi and CaPSi powders. These values can apparently correlate with the surface area, which makes it possible to expect the highest activity for these powders.

Table 2. Weights of prepared powders and by-products.

No.	Labeling	Weight of Prepared Powders, g	Calculated Weight of By-Product, g	Weight of Collected By-Product, g	Difference in Weight of By-Product, g
1	CaP	41.97	42.44	40.01	2.44
2	CaPSi	47.89	42.44	32.89	9.55
3	CaSi	62.76	42.44	22.05	20.39

According to XRD (Figure S1) the phase composition of by-products of all reactions (1–3) isolated from the mother liquors by drying contained only $NaNO_3$.

The phase composition of all synthesized powders after disaggregation in acetone is presented in Figure 1. It should be noted that XRD patterns for powders after synthesis and after disaggregation were the same for each powder. The phase composition of the synthesized powders after the disaggregation process was not changed.

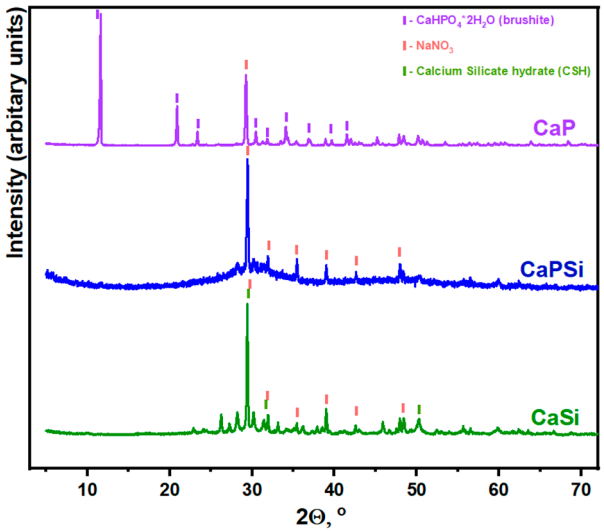

Figure 1. XRD data of powders after synthesis and disaggregation in acetone (CaP, CaPSi, and CaSi). (PDF card 9-77)—brushite, (PDF card 36-1474)—sodium nitrate, (PDF card 33-306)—calcium silicate hydrate.

According to the XRD data (Figure 1), the powder synthesized from $Ca(NO_3)_2$ and Na_2HPO_4 solutions (CaP) after disaggregation contained brushite (dicalcium phosphate dihydrate, $CaHPO_4 \cdot 2H_2O$), as well as the reaction by-product of sodium nitrate ($NaNO_3$).

According to the XRD analysis (Figure 1), the CaSi powder contained crystalline phases of calcium silicate hydrate (CSH) [50] and $NaNO_3$. Under considered synthesis conditions (37 °C and maturation of precipitates during 1 h in the mother liquors), the formation of well-crystallized calcium silicate hydrates (CSH − $Ca_{1.5}SiO_{3.5} \cdot xH_2O$ [PDF card 33-306]) was not expected, since their formation occurs in the process of high-temperature synthesis under autoclave conditions as it is known from the literature [50]. Low-basic hydrosilicates (Ca/Si = 0.8–1.5) have similar peaks on the X-ray diffraction pattern, and weak-crystallized products have 3–4 peaks, which lead to the ambiguous interpretations of the chemical composition. Peaks with interplanar spacing of 3.02A (29.54°) and 1.81A (50.45°) possibly belong to calcium silicate hydrate (CSH), which has a variable Ca/Si ratio from 0.8 to 1.5. The main peaks of CSH are 29.54, 33.25 and 50.45° [50]. And peaks 29.54, 33.25 of CSH overlaps with sodium nitrate peaks. The formation of tobermorite-like gel is also possible [50]. Amorphous calcium phosphate can be stabilized by the presence of silicate ions, as well as calcium silicate hydrate with a Ca/Si ratio from 0.8 to 1.5 [16].

Apparently, the CaPSi powder contained the only crystalline phase of $NaNO_3$. Other phases in the CaPSi powder were calcium silicate hydrate and amorphous calcium phosphate. Taking into account the presence of an amorphous halo near 30° on the XRD pattern of the CaPSi sample, this sample also possibly contained amorphous calcium phosphate (ACP), which could be effectively stabilized in the amorphous state by the presence of a silicate anion [16].

The morphology of the obtained powders after the synthesis and after the disaggregation process is presented in Figure 2.

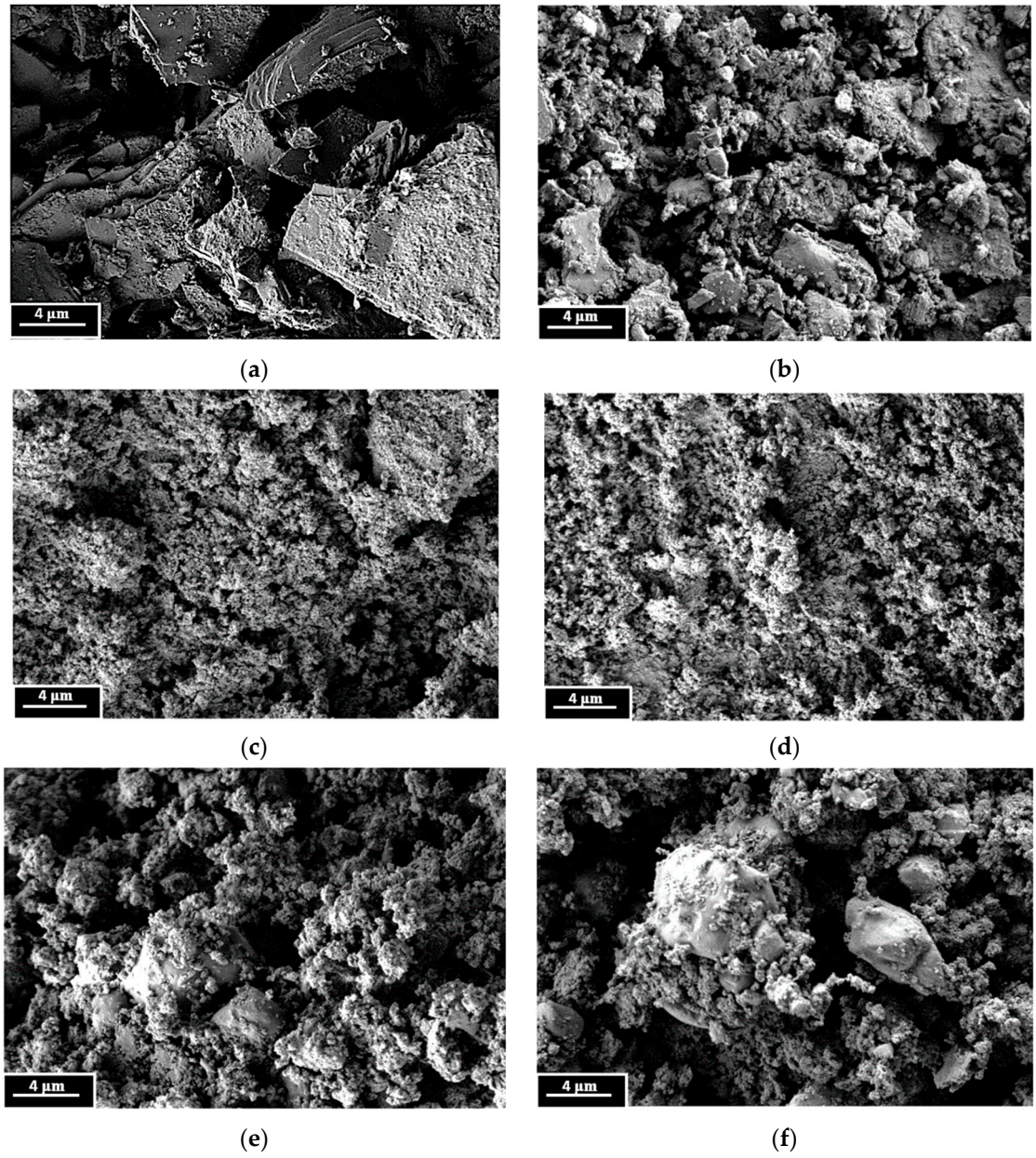

Figure 2. SEM images of powder samples CaP (**a**,**b**), CaPSi (**c**,**d**) and CaSi (**e**,**f**) after synthesis (**a**,**c**,**e**) and disaggregation in acetone (**b**,**d**,**f**).

Brushite crystallizes in the specific shape of large thin bars (longer than 10 µm) characteristic for brushite, which are observed in Figure 2a. This is consistent with the XRD data for CaP powder. After disaggregation, elongated lamellar particles with a size of 1–2 µm remained (Figure 2b).

Large spheroid aggregates with dimensions 4–8 µm are presented in the SEM images of the CaSi powder sample before and after disaggregation (Figure 2e,f). The dimensions of particles in aggregates before and after disaggregation were not bigger than 50 nm. Apparently, this morphology corresponds to the presence of amorphous calcium silicate hydrate.

The CaPSi sample of synthesized powder is also consisted of aggregates (4–8 µm) of spheroid particles (~50 nm), as it is shown by the SEM image (Figure 2c). These spheroid particles may consist of amorphous phase of both hydrated ACP and calcium silicate hydrate. After disaggregation, the powders contain mesoporous aggregates (2–4 µm) of spherical particles of submicron (~50 nm) size (Figure 2d). Thereby, implementation

of synthesis via precipitation from mixed-anion solution (CaPSi sample) leads to the production of powders consisted of submicron particles, which are smaller than those reported in previous studies, where the powders were obtained using another method [51].

According to the TG data, the final mass loss of the CaP powder after heating to 1000 °C was 28.3% (Figure 3a). At the first stage (up to 160 °C), there was a gradual decomposition of structurally unbonded water, accompanied by a slight endoeffect. At the next stage (up to 200 °C), the transition of brushite to monetite (DCPD → DCPA (dicalcium phosphate anhydrous)) occurred, accompanied by a significant endoeffect with a maximum at 190 °C (Figure 3b). The further process is the transformation of monetite to γ-pyrophosphate (DCPA → γ-CPP), generally takes place at 400 °C. But the process of transformation of DCPA to CPP in powder CaP under investigation tooks place at lower temperature. The mass loss takes place with an endoeffect at 295 °C (Figure 3b). This endoeffect may also be associated with the melting of sodium nitrate (melting point – 308 °C). So, we can state that the presence of monetite can make the melting point of sodium nitrate lower and consequently the presence of the melt of sodium nitrate leads to the thermal transformation (DCPA → CPP) at lower temperature. According to XRD data (Figure 4,a, Table 3) after heart treatment at 400 °C the phase composition of CaP powder included β-$Ca_2P_2O_7$ and $NaNO_3$. So, the transition of the γ-phase to the β-phase (γ-CPP → β-CPP) also was facilitated and made a contribution in the appearance of endoeffect in interval 250–350 °C. The next step of mass loss with endoeffect at 503 °C can be explained by sodium rhenanite formation from calcium pyrophosphate and sodium nitrate as it was confirmed by XRD data for powder CaP after heat treatment at 600 °C (Figure 4a, Table 3). The maximum endoeffect at the temperature of 503 °C corresponds to the maximum at 500 °C in interval 400–560 °C at mass-spectroscopy graph (Figure S2) by NO ion current (NO (M = 30) release) and the formation of the sodium rhenanite phase according to the formal reaction (6), which is not reflect the complicity of the thermal decomposition of nitrates.

$$Ca_2P_2O_7 + 2NaNO_3 \rightarrow 2NaCaPO_4 + N_2O_5 \quad (6)$$

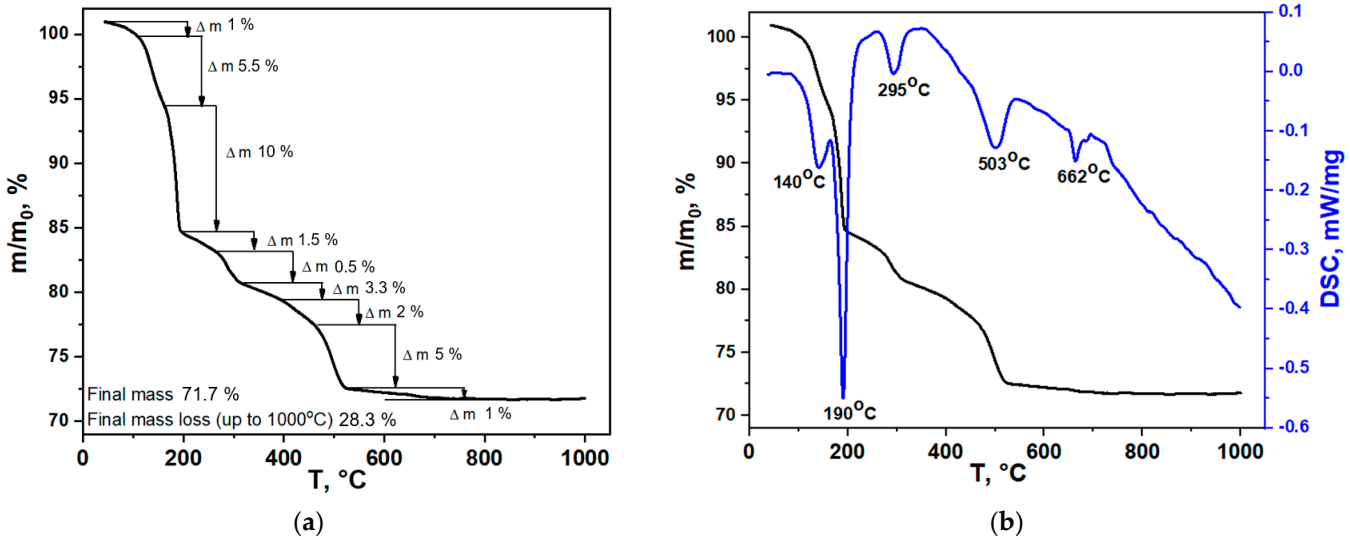

Figure 3. *Cont.*

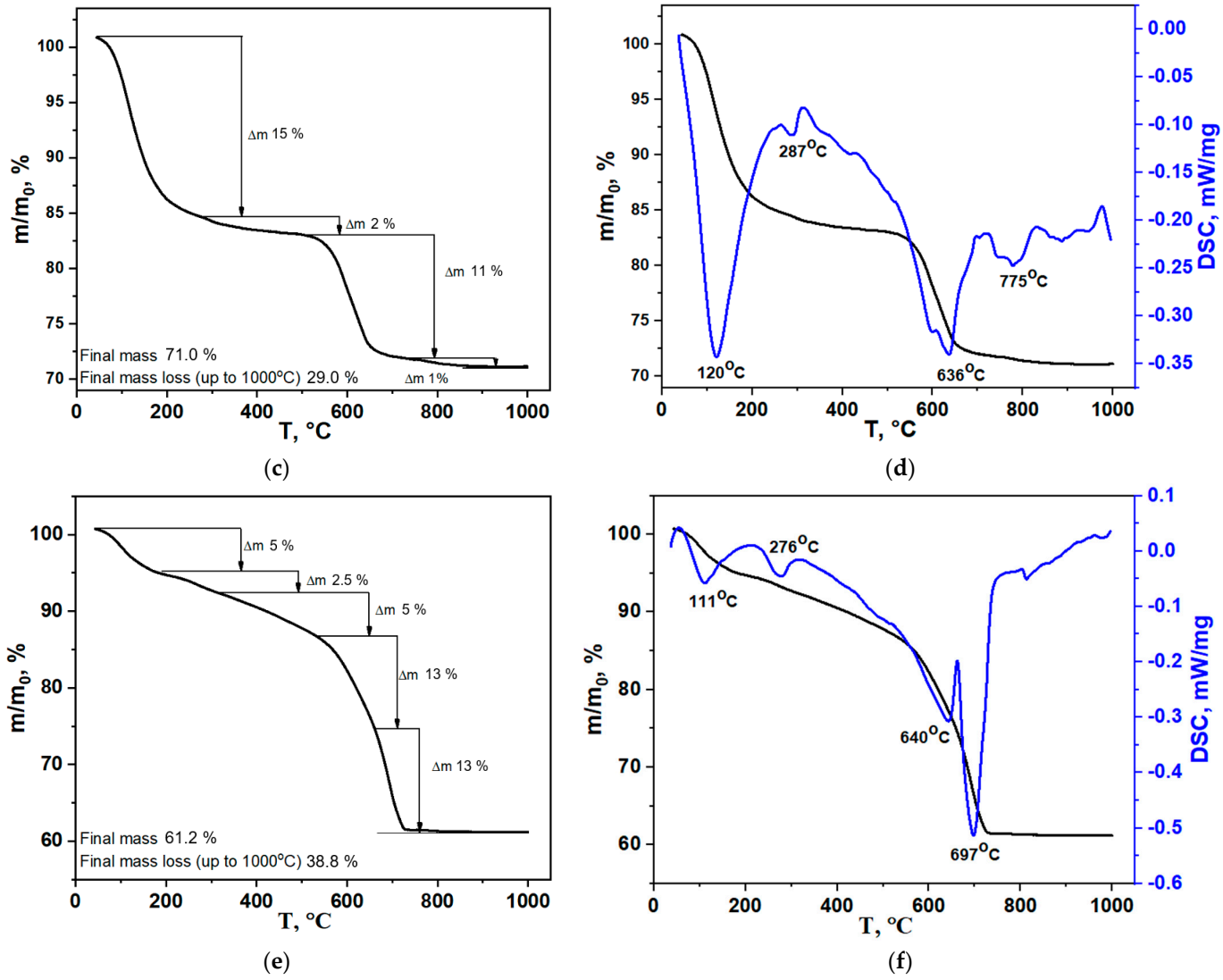

Figure 3. (**a**) step change in mass, and (**b**) TG/DTA curves obtained for the CaP synthesized powders; (**c**) step change in mass, and (**d**) TG/DTA curves obtained for the CaPSi synthesized powders, and (**e**) step change in mass, and (**f**) TG/DTA curves obtained for the CaSi synthesized powders.

Table 3. Transformation of the phase composition of preceramic and ceramic samples after heat treatment at specified temperature for 2 h.

Sample	Heat Treatment Temperature, °C				
	400	600	800	900	1000
CaP	β-$Ca_2P_2O_7$ $NaNO_3$	β-$Ca_2P_2O_7$ β-$NaCaPO_4$	β-$Ca_2P_2O_7$ β-$NaCaPO_4$	β-$Ca_2P_2O_7$ β-$NaCaPO_4$	β-$Ca_2P_2O_7$ β-$NaCaPO_4$
CaPSi	$Ca_5(PO_4)_3OH$ $NaNO_3$ α-$CaSiO_3$	β-$NaCaPO_4$ $Ca_5(PO_4)_3OH$ α-$CaSiO_3$	β-$NaCaPO_4$ $Ca_5(PO_4)_3OH$ α-$CaSiO_3$ $Na_3Ca_6(PO_4)_5$	β-$NaCaPO_4$ α-$CaSiO_3$ $Na_3Ca_6(PO_4)_5$	β-$NaCaPO_4$ α-$CaSiO_3$ $Na_3Ca_6(PO_4)_5$
CaSi	CSH $NaNO_3$	CSH $NaNO_3$ $Ca_5Si_6O_{16}(OH)_2$ $Na_6Ca_3Si_6O_{18}$	α-$CaSiO_3$ $Na_2Ca_2Si_2O_7$	α-$CaSiO_3$ $Na_2Ca_2Si_2O_7$	α-$CaSiO_3$ $Na_2Ca_2Si_2O_7$

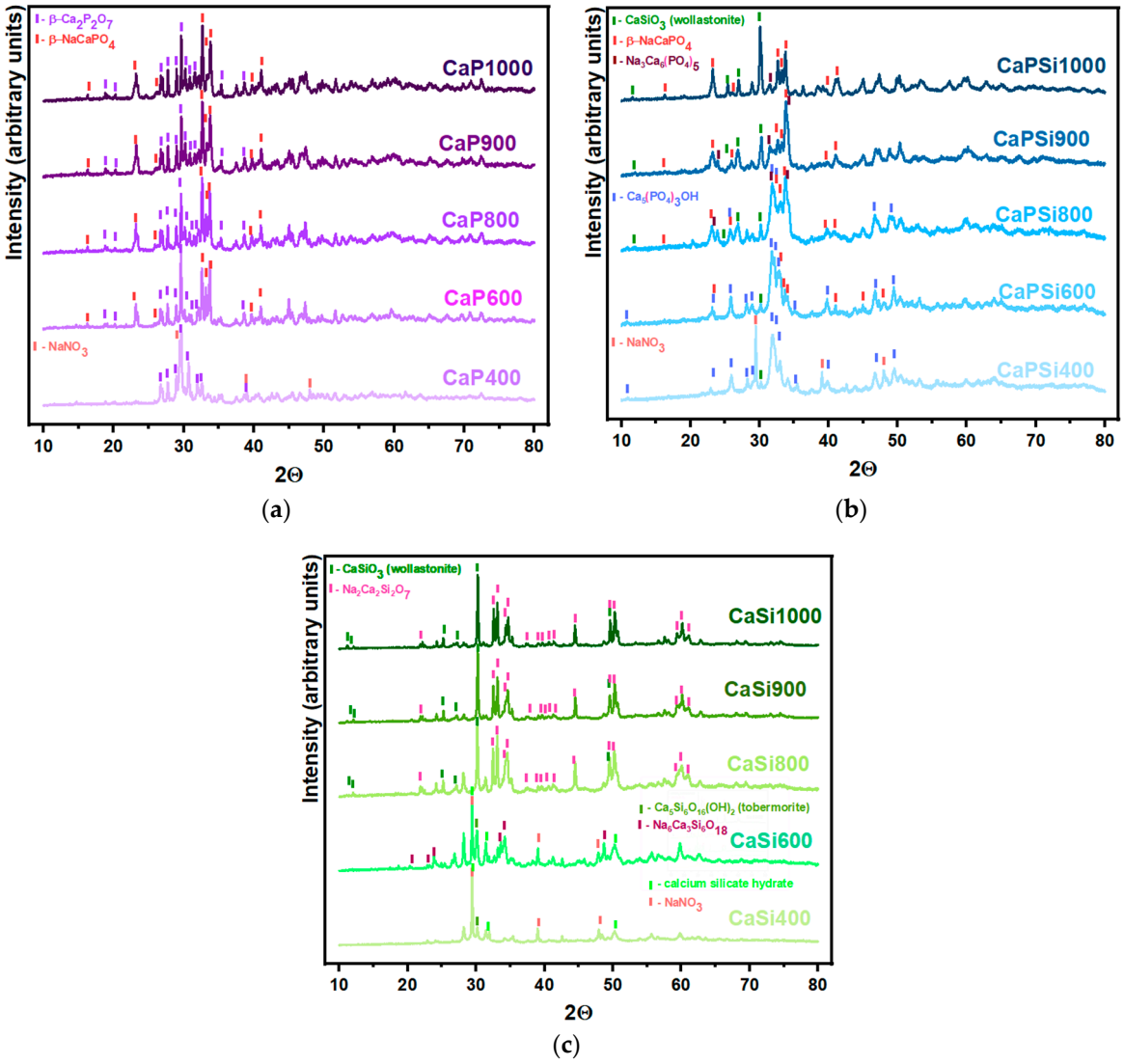

Figure 4. XRD patterns of CaP (**a**), CaSi (**b**), and CaPSi (**c**) samples after heat treatment at 1000 °C; CaPSi samples after heat treatment at 800, 900, and 1000 °C. (9-346)—$Ca_2P_2O_7$—purple, (29-1193)—$NaCaPO_4$—red, (76-186)—α-$CaSiO_3$—green, (10-16)—$Na_2Ca_2Si_2O_7$—pink, (11-236)—$Na_3Ca_6(PO_4)_5$—dark red.

For the CaSi sample, the final mass loss after heating to 1000 °C was 38.8% (Figure 3d). The first endoeffect (Figure 3e) at a temperature of 100–120 °C was apparently due to the elimination of structurally unbonded water. The endoeffect at the temperature of 300–310 °C was associated with the melting of sodium nitrate (melting point - 308 °C). Apparently, then there was a gradual crystallization of the amorphous phase with the formation of α-$CaSiO_3$ (wollastonite), including the possible formation of the intermediate tobermarite phase at 400–500 °C, up to 650 °C (with a significant endoeffect on the DSC graph). Confirmation of the gradual formation of wollastonite is presented in Figure 4c. The formation of wollastonite apparently continues up to 800 °C (Table 3). The maximum endoeffect at a temperature of 700 °C can be associated with the complete decomposition of sodium nitrate, which was also observed at the corresponding mass-spectroscopy graphs (Figure S2) by NO ion current (NO (M = 30) release) and the formation of the $Na_2Ca_2Si_2O_7$ phase (Figure 3f) and the sodium rhenanite phase (Figure 3b,d). The temperature of NO release depends on the composition of the sample. This indirectly indicates the surface area of powder that possibly holds the by-product. Thus, CaSi has the largest surface area, the maximum content of the by-product (Table 2) and a higher temperature, which

is required to detach the nitrate. The ratio of intensity values of ion current for m/Z = 30 (NO) also indicates an increase in the content of sodium nitrate in the samples in the series CaP-CaPSi-CaSi (correspondingly 0.70×10^{-12}, 1.06×10^{-12}, 2.57×10^{-12}). The NO release peak for this series shifts to higher temperatures. Thus, the reactivity of CaP powder is higher than that of CaSi powder.

The total mass loss of the CaPSi sample after heating to 1000 °C was 29.0% (Figure 3b). Two steps of mass loss (17% and 12%) can be observed at the TG curve. According to MS data one step is connected with H_2O release up to 420 °C. And the second step is observed due to the processes connected with the decomposition of sodium nitrate or with heterphase reactions with sodium nitrate in the interval 450–750 °C. DTA graph (Figure 3c) clearly shows that two significant endoeffects corresponds to these steps of mass loss. According to XRD data for CaPSi sample after heat treatment at 400 and 600 °C hydroxyapatite, sodium nitrate and wollastonite was found. Up to 250 °C, the formation of the hydroxyapatite phase occurs from the amorphous calcium phosphate [52], as well as the beginning of the wollastonite phase forming, which apparently lasts up to 800 °C and also causes a 2% mass change in the temperature range 250–500 °C [25]. After 500 °C, the formation of the $Na_3Ca_6(PO_4)_5$ phase, and the sodium rhenanite (β-$NaCaPO_4$) phase occurs (Figure 3d).

As discussed above, heat treatment of the CaP powder at 600 °C and the ceramic samples at the range of temperatures from 800 to 1000 °C leads to the formation of a two-phase powder and ceramic samples containing calcium pyrophosphate (β-$Ca_2P_2O_7$) and β-rhenanite (β-$NaCaPO_4$). No other phases were found in the considered quasi-binary system [29].

In the case of the CaSi sample after the thermal treatment at 400 °C, there were no significant changes in phase composition, in comparison with the phase composition before the thermal treatment. After the thermal treatment at 600 °C, the formation of $Ca_5Si_6O_{16}(OH)_2$ and $Na_6Ca_3Si_6O_{18}$ occurred. Two-phase composite ceramics including wollastonite (α-CaSiO3) and $Na_2Ca_2Si_2O_7$ (Table 3, Figure 4; ICDD PDF2 database [53]) were also obtained after heat treatment of the CaSi samples at the range from 800 to 1000 °C.

After the heat treatment at 400 °C, the formation of hydroxyapatite and wollastonite occurred for the CaPSi sample. Presence of H_2O at high temperature give us an opportunity to guess that hydroxyapatite was formed under hydrothermal conditions. At 600 °C, the formation of hydroxyapatite from the amorphous phase, accompanied with the formation of sodium rhenanite from the amorphous phase and $NaNO_3$, occurred. The heat treatment at 800 °C led to the formation of tetraphasic ceramics, containing sodium rhenanite, hydroxyapatite, wollastonite and the $Na_3Ca_6(PO_4)_5$ phase. The phase composition of the CaPSi ceramic samples after the heat treatment in the range of temperatures from 900 to 1000 °C (Figure 4b, Table 3) remained almost unchanged. These samples after heat treatments at 900 and 1000 °C contained wollastonite (α-$CaSiO_3$), sodium rhenanite ($NaCaPO_4$), and mixed calcium-sodium phosphate ($Na_3Ca_6(PO_4)_5$). Nevertheless, the phase ratios varied depending on the heat treatment temperature. With an increase in the heat treatment temperature the phases tended to become more crystallized. The reflexes of the wollastonite (α-$CaSiO_3$) phase increased in the range of temperatures from 800 to 1000 °C, while the hydroxyapatite phase disappeared. After this temperature, heterophase reactions between hydroxyapatite and sodium rhenanite occurred, leading to the formation of $Na_3Ca_6(PO_4)_5$.

The SEM images of the surface of ceramic samples sintered at 1000 °C are shown in Figure 5.

With an increase in the heat treatment temperature, the sintering of the samples proceeds more efficiently due to the elimination of pores and the growth of grains, the size of which is 8–10 μm when fired at 1000 °C (CaP), while the grain sizes for the other samples are 2–3 μm (CaSi) and 2–4 μm (CaPSi).

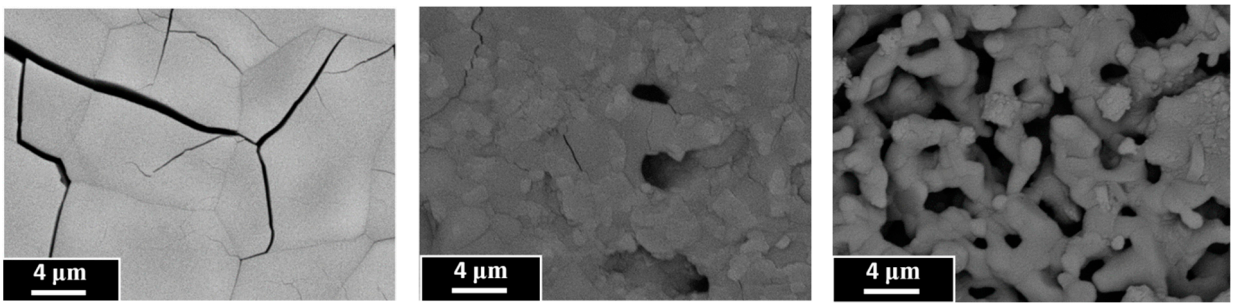

(**a**) (**b**) (**c**)

Figure 5. SEM images of ceramics obtained from powders (**a**) CaP; (**b**) CaPSi; (**c**) CaSi after heat treatment at 1000 °C.

Apparently, the occurrence of heterophase reactions in the CaSi and CaPSi samples inhibits grain growth in ceramics. The formation of sodium rhenanite and pyrophosphate is completed already after the heat treatment at 600 °C. During the heat treatment at higher temperatures, grain growth is possible since there are no conditions for heterophase reactions in the quasi-binary calcium pyrophosphate-sodium rhenanite system.

With an increase in the heat treatment temperature (and in the content of wollastonite), the ceramics became denser, which was accompanied by a significant grain growth up to 2–4 µm from submicron size. Microporosity of CaPSi also disappeared and a small number of pores with a diameter of 2–3 µm were formed. The ceramics based on the CaSi powder were highly porous, which was consistent with the literature data [54].

The shrinkage density of the samples CaP, CaPSi, and CaSi during the heat treatment is presented in Figure 6. The initial density of all the powder pre-ceramic samples in the form of disks was approximately equal and was 1.30 g/cm^3 for CaP and CaSi and 1.20 g/cm^3 for CaPSi.

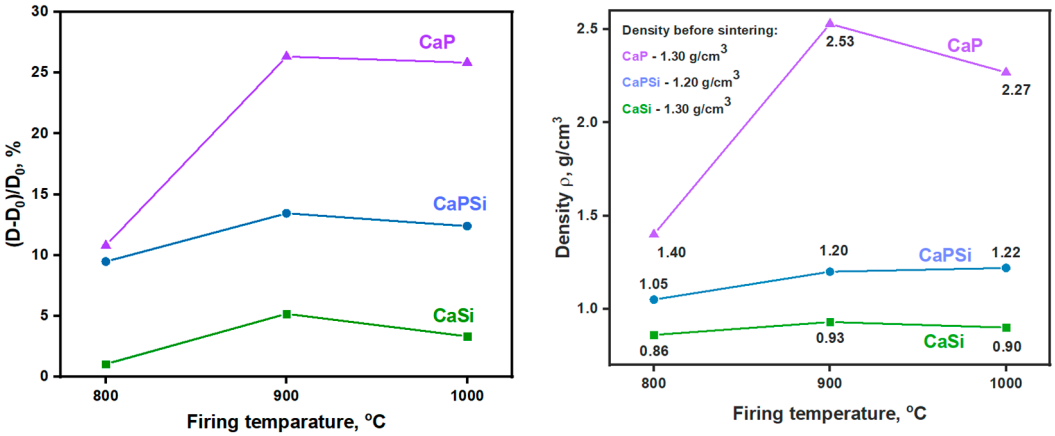

(**a**) (**b**)

Figure 6. (**a**) Shrinkage during heat treatment, and (**b**) density of samples CaP, CaSi, and CaSi.

The CaP sample had the largest linear shrinkage (up to 26% at 900 and 1000 °C), and the CaSi sample had the smallest linear shrinkage (up to 5%) (Figure 6a). Linear shrinkage for the CaPSi sample ranged from 9 to 13% at 800 to 1000 °C, respectively. At the same time, fluctuations in density changes depending on the temperature for the CaPSi samples are minor, since the obtained components have approximately the same density (1.05–1.22 g/cm^3).

The apparent densities of the obtained ceramics are consistent with the scanning electron microscopy data (Figure 6b). The CaP sample fired at 900 and 1000 °C had the highest density. The uniform distribution of cracks visible on the surface of the CaP ceramic sample was apparently caused by the phase transformation in sodium rhenanite.

4. Conclusions

A novel method of multi-component active powders production was proposed in this work. The powders were prepared using a synthesis from aqueous solutions of $CaNO_3$ and a mixed-anion solution containing Na_2HPO_4 and Na_2SiO_3. For comparison, the powders were synthesized from solutions of $CaNO_3$ and solutions containing these sodium salts separately.

Phase composition of the CaP powder included brushite $CaHPO_4 \cdot 2H_2O$ and the CaSi powder included calcium silicate hydrate. Phase composition of the CaPSi powder consisted of the amorphous phase (presumably containing hydrated quasi-amorphous calcium phosphate and calcium silicate phase). All synthesized powders contained $NaNO_3$ as a by-product. The quasi-amorphous phases of CaPSi powder, obtained by precipitation from mixed-anionic solution, as it can be assumed, stabilized each other. A significant amount of by-product $NaNO_3$ was intentionally kept in the composition of all obtained powders for the synthesis of the ceramics of the Na_2O-CaO-SiO_2-P_2O_5 system during heat treatment of samples. This component acts both as a sintering aid and as a participant of the heterophase reactions of the formation of the ceramics based on the prepared powders (CaP. CaPSi, CaSi). The obtained powders were used to produce ceramics by the heat treatment at 800, 900, and 1000 °C. The main phases obtained for the ceramics based on the CaPSi powder were β-rhenanite β-$NaCaPO_4$, wollastonite α-$CaSiO_3$ and $Na_3Ca_6(PO_4)_5$. The density of the CaPSi ceramics increased with the heat treatment temperature from 1.47 g/cm^3 (800 °C) to 1.72 g/cm^3 (1000 °C). The ceramics based on the CaP powder had the highest density (2.53 g/cm^3) after the heat treatment at 900 °C. The ceramics based on the CaSi powder were significantly porous and had the lowest density (1.52 g/cm^3) after the heat treatment at 900 °C. The ceramics prepared in this work in the CaO-SiO_2-P_2O_5-Na_2O system and containing the biocompatible and bioresorbable phases can be recommended for use in medicine for bone defect treatment. The obtained materials are expected to support cell proliferation and differentiation. Osteoconductive 3D forms also can be manufactured from obtained powders.

Supplementary Materials: The following supporting information can be downloaded at: https://www.mdpi.com/article/10.3390/coatings13020374/s1, Figure S1: XRD data of by-product powders dried from solutions, collected after filtration (mother liquors) (PDF card 36-1474)–sodium nitrate, Figure S2: Mass-spectroscopy data of (a) CaP, (b) CaPSi, (c) CaSi powders.

Author Contributions: Conceptualization, D.G. and T.V.S.; methodology, D.G. and T.V.S.; validation, D.G., E.N. and T.V.S.; investigation, D.G., E.N., T.V.S., T.B.S., I.N.T., I.V.R., D.K., V.P., O.B., M.K., D.A.F. and K.A.L.; resources, T.B.S., I.V.R., O.B. and K.A.L.; data curation, D.G. and E.N.; writing—original draft preparation, D.G. and E.N.; writing—review and editing, D.G., E.N. and T.V.S.; visualization, D.G., E.N., T.B.S., I.V.R., D.K., V.P., O.B. and M.K.; supervision, T.V.S.; funding acquisition, T.V.S. All authors have read and agreed to the published version of the manuscript.

Funding: This work was carried out with financial support from the Russian Science Foundation (grant no. 22-19-00219).

Institutional Review Board Statement: Not applicable.

Informed Consent Statement: Not applicable.

Data Availability Statement: Not applicable.

Acknowledgments: This research was carried out using the equipment of the MSU Shared Research Equipment Center "Technologies for obtaining new nanostructured materials and their complex study" and purchased by MSU in the frame of the Equipment Renovation Program (National Project "Science"), and in the frame of the MSU Program of Development. The authors would like to thank Elena Golubchikova for the assistance with draft preparation. Some of the SEM images were recorded using scientific equipment at the Joint Research Center for Physical Methods of Research, located in the Kurnakov Institute of General and Inorganic Chemistry RAS.

Conflicts of Interest: The authors declare no conflict of interest.

References

1. Stevens, M.M. Biomaterials for Bone Tissue Engineering. *Mater. Today* **2008**, *11*, 18–25. [CrossRef]
2. Ansari, M. Bone Tissue Regeneration: Biology, Strategies and Interface Studies. *Prog. Biomater.* **2019**, *8*, 223–237. [CrossRef]
3. Ashammakhi, N.; Hasan, A.; Kaarela, O.; Byambaa, B.; Sheikhi, A.; Gaharwar, A.K.; Khademhosseini, A. Advancing Frontiers in Bone Bioprinting. *Adv. Healthc. Mater.* **2019**, *8*, 1801048. [CrossRef] [PubMed]
4. Amiryaghoubi, N.; Fathi, M.; Pesyan, N.N.; Samiei, M.; Barar, J.; Omidi, Y. Bioactive Polymeric Scaffolds for Osteogenic Repair and Bone Regenerative Medicine. *Med. Res. Rev.* **2020**, *40*, 1833–1870. [CrossRef] [PubMed]
5. Shuai, C.; Yang, W.; Feng, P.; Peng, S.; Pan, H. Accelerated Degradation of HAP/PLLA Bone Scaffold by PGA Blending Facilitates Bioactivity and Osteoconductivity. *Bioact. Mater.* **2021**, *6*, 490–502. [CrossRef]
6. Yamada, Y.; Inui, T.; Kinoshita, Y.; Shigemitsu, Y.; Honda, M.; Nakano, K.; Matsunari, H.; Nagaya, M.; Nagashima, H.; Aizawa, M. Silicon-Containing Apatite Fiber Scaffolds with Enhanced Mechanical Property Express Osteoinductivity and High Osteoconductivity. *J. Asian Ceram. Soc.* **2019**, *7*, 101–108. [CrossRef]
7. Malhotra, A.; Habibovic, P. Calcium Phosphates and Angiogenesis: Implications and Advances for Bone Regeneration. *Trends Biotechnol.* **2016**, *34*, 983–992. [CrossRef] [PubMed]
8. Schmidt-Bleek, K.; Schell, H.; Schulz, N.; Hoff, P.; Perka, C.; Buttgereit, F.; Volk, H.-D.; Lienau, J.; Duda, G.N. Inflammatory Phase of Bone Healing Initiates the Regenerative Healing Cascade. *Cell Tissue Res.* **2012**, *347*, 567–573. [CrossRef] [PubMed]
9. Ligon, S.C.; Liska, R.; Stampfl, J.; Gurr, M.; Mülhaupt, R. Polymers for 3D Printing and Customized Additive Manufacturing. *Chem. Rev.* **2017**, *117*, 10212–10290. [CrossRef]
10. Mao, M.; He, J.; Li, X.; Zhang, B.; Lei, Q.; Liu, Y.; Li, D. The Emerging Frontiers and Applications of High-Resolution 3D Printing. *Micromachines* **2017**, *8*, 113. [CrossRef]
11. Pina, S.; Ribeiro, V.P.; Marques, C.F.; Maia, F.R.; Silva, T.H.; Reis, R.L.; Oliveira, J.M. Scaffolding Strategies for Tissue Engineering and Regenerative Medicine Applications. *Materials* **2019**, *12*, 1824. [CrossRef] [PubMed]
12. Yunus Basha, R.; Kumar, T.S.S.; Doble, M. Design of Biocomposite Materials for Bone Tissue Regeneration. *Mater. Sci. Eng. C* **2015**, *57*, 452–463. [CrossRef] [PubMed]
13. Guzzo, C.M.; Nychka, J.A. Bone 'Spackling' Paste: Mechanical Properties and In Vitro Response of a Porous Ceramic Composite Bone Tissue Scaffold. *J. Mech. Behav. Biomed. Mater.* **2020**, *112*, 103958. [CrossRef] [PubMed]
14. Guzzo, C.M.; Nychka, J. Fabrication of a Porous and Formable Ceramic Composite Bone Tissue Scaffold at Ambient Temperature. *Metall. Mater. Trans. A* **2020**, *51*, 6110–6126. [CrossRef]
15. Kazakova, G.; Safronova, T.; Golubchikov, D.; Shevtsova, O.; Rau, J.V. Resorbable Mg^{2+}-Containing Phosphates for Bone Tissue Repair. *Materials* **2021**, *14*, 4857. [CrossRef]
16. Zuev, D.M.; Golubchikov, D.O.; Evdokimov, P.V.; Putlyaev, V.I. Synthesis of Amorphous Calcium Phosphate Powders for Production of Bioceramics and Composites by 3D Printing. *Russ. J. Inorg. Chem.* **2022**, *67*, 940–951. [CrossRef]
17. Koons, G.L.; Diba, M.; Mikos, A.G. Materials Design for Bone-Tissue Engineering. *Nat. Rev. Mater.* **2020**, *5*, 584–603. [CrossRef]
18. Hu, X.; Wang, Y.; Tan, Y.; Wang, J.; Liu, H.; Wang, Y.; Yang, S.; Shi, M.; Zhao, S.; Zhang, Y.; et al. A Difunctional Regeneration Scaffold for Knee Repair Based on Aptamer-Directed Cell Recruitment. *Adv. Mater.* **2017**, *29*, 1605235. [CrossRef]
19. Hench, L.L.; Splinter, R.J.; Allen, W.C.; Greenlee, T.K. Bonding Mechanisms at the Interface of Ceramic Prosthetic Materials. *J. Biomed. Mater. Res.* **1971**, *5*, 117–141. [CrossRef]
20. Hench, L.L.; Paschall, H.A. Direct Chemical Bond of Bioactive Glass-Ceramic Materials to Bone and Muscle. *J. Biomed. Mater. Res.* **1973**, *7*, 25–42. [CrossRef]
21. Li, H.; Xue, K.; Kong, N.; Liu, K.; Chang, J. Silicate Bioceramics Enhanced Vascularization and Osteogenesis through Stimulating Interactions between Endothelia Cells and Bone Marrow Stromal Cells. *Biomaterials* **2014**, *35*, 3803–3818. [CrossRef]
22. Kaully, T.; Kaufman-Francis, K.; Lesman, A.; Levenberg, S. Vascularization—The Conduit to Viable Engineered Tissues. *Tissue Eng. Part B Rev.* **2009**, *15*, 159–169. [CrossRef] [PubMed]
23. Hillert, M.; Sundman, B.; Wang, X. An Assessment of the CaO-SiO_2 System. *Metall. Mater. Trans. B* **1990**, *21*, 303–312. [CrossRef]
24. Fu, S.; Liu, W.; Liu, S.; Zhao, S.; Zhu, Y. 3D Printed Porous β-Ca_2SiO_4 Scaffolds Derived from Preceramic Resin and Their Physicochemical and Biological Properties. *Sci. Technol. Adv. Mater.* **2018**, *19*, 495–506. [CrossRef]
25. Pan, Y.; Yin, J.; Yao, D.; Zuo, K.; Xia, Y.; Liang, H.; Zeng, Y. Effects of Silica Sol on the Microstructure and Mechanical Properties of CaSiO3 Bioceramics. *Mater. Sci. Eng. C.* **2016**, *64*, 336–340. [CrossRef]
26. De Aza, P.N.; Luklinska, Z.B.; Martinez, A.; Anseau, M.R.; Guitian, F.; De Aza, S. Morphological and Structural Study of Pseudowollastonite Implants in Bone. *J. Microsc.* **2000**, *197*, 60–67. [CrossRef]
27. Yu, Q.; Chang, J.; Wu, C. Silicate Bioceramics: From Soft Tissue Regeneration to Tumor Therapy. *J. Mater. Chem. B* **2019**, *7*, 5449–5460. [CrossRef]
28. Hu, Y.; Xiao, Z.; Wang, H.; Ye, C.; Wu, Y.; Xu, S. Fabrication and Characterization of Porous $CaSiO_3$ Ceramics. *Ceram. Int.* **2019**, *45*, 3710–3714. [CrossRef]
29. Filippov, Y.; Murashko, A.; Evdokimov, P.; Safronova, T.; Putlayev, V. Stereolithography 3D printed calcium pyrophosphate macroporous ceramics for bone grafting. *Open Ceram.* **2021**, *8*, 100185. [CrossRef]
30. Serena, S.; Sainz, M.; Caballero, A. Single-phase silicocarnotite synthesis in the subsystem $Ca_3(PO_4)_2$–Ca_2SiO_4. *Ceram. Int.* **2014**, *40*, 8245–8252. [CrossRef]

31. Ros-Tarraga, P.; Mazon, P.; Meseguer-Olmo, L.; De Aza, P. Revising the Subsystem Nurse's A-Phase-Silicocarnotite within the System $Ca_3(PO_4)_2$–Ca_2SiO_4. *Materials* **2016**, *9*, 322. [CrossRef] [PubMed]
32. Xu, M.; Zhai, D.; Chang, J.; Wu, C. In Vitro assessment of three-dimensionally plotted nagelschmidtite bioceramic scaffolds with varied macropore morphologies. *Acta Biomater.* **2014**, *10*, 463–476. [CrossRef]
33. Anand, V.; Singh, K.; Kaur, K. Investigation of Mg and Zn doped 45S5 bioactive materials by XRD, FTIR and SEM techniques. *AIP Conf. Proc.* **2014**, *1591*, 745. [CrossRef]
34. Zhang, X.; Guo, X.; Zhang, J.; Fan, X.; Chen, M.; Yang, H. Nucleation, Crystallization and Biological Activity of Na_2O-CaO-P_2O_5-SiO_2 Bioactive Glass. *J. Non Cryst. Solids* **2021**, *568*, 120929. [CrossRef]
35. Kahlenberg, V.; Hösch, A. The Crystal Structure of $Na_2Ca_2Si_2O_7$—A Mixed Anion Silicate with Defect Perovskite Characteristics. *Z. Krist. Cryst. Mater.* **2002**, *217*, 155–163. [CrossRef]
36. Leenakul, W.; Pisitpipathsin, N.; Kantha, P.; Tawichai, N.; Tigunta, S.; Eitssayeam, S.; Rujijanagul, G.; Pengpat, K.; Munpakdee, A. Characteristics of 45S5 Bioglass-Ceramics Using Natural Raw Materials. *AMR Adv. Mater. Res.* **2012**, *506*, 174–177. [CrossRef]
37. Kaimonov, M.; Safronova, T.; Shatalova, T.; Filippov, Y.; Tikhomirova, I.; Sergeev, N. Composite Ceramics in the Na_2O–CaO–SiO_2–$P2O_5$ System Obtained from Pastes Including Hydroxyapatite and an Aqueous Solution of Sodium Silicate. *Ceramics* **2022**, *5*, 550–561. [CrossRef]
38. Safronova, T.V. Inorganic Materials for Regenerative Medicine. *Inorg. Mater.* **2021**, *57*, 443–474. [CrossRef]
39. Demirkiran, H.; Mohandas, A.; Dohi, M.; Fuentes, A.; Nguyen, K.; Aswath, P. Bioactivity and Mineralization of Hydroxyapatite with Bioglass as Sintering Aid and Bioceramics with $Na_3Ca_6(PO_4)_5$ and $Ca_5(PO_4)_2SiO_4$ in a Silicate Matrix. *Mater. Sci. Eng. C* **2010**, *30*, 263–272. [CrossRef]
40. Lin, K.; Zhai, W.; Ni, S.; Chang, J.; Zeng, Y.; Qian, W. Study of the Mechanical Property and In Vitro Biocompatibility of $CaSiO_3$ Ceramics. *Ceram. Int.* **2005**, *31*, 323–326. [CrossRef]
41. Gmeiner, R.; Deisinger, U.; Schönherr, J.; Lechner, B.; Detsch, R.; Boccaccini, A.R.; Stampfl, J. Additive Manufacturing of Bioactive Glasses and Silicate Bioceramics. *J. Ceram. Sci. Technol.* **2015**, *6*, 75–86. [CrossRef]
42. Bergmann, C.; Lindner, M.; Zhang, W.; Koczur, K.; Kirsten, A.; Telle, R.; Fischer, H. 3D Printing of Bone Substitute Implants Using Calcium Phosphate and Bioactive Glasses. *J. Eur. Ceram. Soc.* **2010**, *30*, 2563–2567. [CrossRef]
43. Safronova, T.V.; Knot'ko, A.V.; Shatalova, T.B.; Evdokimov, P.V.; Putlyaev, V.I.; Kostin, M.S. Calcium phosphate ceramic based on powder synthesized from a mixed-anionic solution. *Glass Ceram.* **2016**, *73*, 25–31. [CrossRef]
44. Peranidze, K.; Safronova, T.V.; Filippov, Y.; Kazakova, G.; Shatalova, T.; Rau, J.V. Powders Based on $Ca_2P_2O_7$-$CaCO_3$-H_2O System as Model Objects for the Development of Bioceramics. *Ceramics* **2022**, *5*, 423–434. [CrossRef]
45. Safronova, T.V.; Putlyaev, V.I.; Filippov, Y.Y.; Knot'Ko, A.V.; Klimashina, E.S.; Peranidze, K.K.; Evdokimov, P.V.; Vladimirova, S.A. Powders Synthesized from Calcium Acetate and Mixed-Anionic Solutions, Containing Orthophosphate and Carbonate Ions, for Obtaining Bioceramic. *Glass Ceram.* **2018**, *75*, 118–123. [CrossRef]
46. Joksa, A.A.; Komarovska, L.; Ubele-Kalnina, D.; Viksna, A.; Gross, K.A. Role of carbonate on the crystallization and processing of amorphous calcium phosphates. *Materialia* **2023**, *27*, 101672. [CrossRef]
47. Safronova, T.V.; Putlyaev, V.I.; Filippov, Y.; Shatalova, T.B.; Fatin, D.S. Ceramics based on brushite powder synthesized from calcium nitrate and disodium and dipotassium hydrogen phosphates. *Inorg. Mater.* **2018**, *54*, 195–207. [CrossRef]
48. Safronova, T.V. Phase Composition of Ceramic Based on Calcium Hydroxyapatite Powders Containing Byproducts of the Synthesis Reaction. *Glass Ceram.* **2009**, *66*, 136–139. [CrossRef]
49. Safronova, T.V.; Putlyaev, V.I.; Knot'ko, A.V.; Shatalova, T.B.; Artemov, M.V.; Filippov, Y.Y. Properties of Calcium Phosphate Powder Synthesized from Calcium Chloride and Potassium Pyrophosphate. *Inorg. Mater. Appl. Res.* **2020**, *11*, 44–49. [CrossRef]
50. Gorshkov, V.; Timashev, V.; Saveliev, V. Identification characteristics of compounds containing water. In *Methods for Physical and Chemical Analysis of Binders*; Gaidzhurov, P., Nekrasov, K., Eds.; Vyshaya Shkola: Moscow, Russia, 1981; pp. 292–294. (In Russian)
51. Solonenko, A.P.; Blesman, A.I.; Polonyankin, D.A.; Gorbunov, V.A. Synthesis of Calcium Phosphate and Calcium Silicate Composites. *Russ. J. Inorg. Chem.* **2018**, *63*, 993–1000. [CrossRef]
52. Vecstaudza, J.; Gasik, M.; Locs, J. Amorphous Calcium Phosphate Materials: Formation, Structure and Thermal Behaviour. *J. Eur. Ceram. Soc.* **2019**, *39*, 1642–1649. [CrossRef]
53. ICDD. *PDF-4+ Database*; Kabekkodu, S., Ed.; International Centre for Diffraction Data: Newtown Square, PA, USA, 2010. Available online: https://www.icdd.com/pdf-2/ (accessed on 20 February 2022).
54. Li, L.; Hu, H.; Zhu, Y.; Zhu, M.; Liu, Z. 3D-Printed Ternary SiO_2CaO P_2O_5 Bioglass-Ceramic Scaffolds with Tunable Compositions and Properties for Bone Regeneration. *Ceram. Int.* **2019**, *45*, 10997–11005. [CrossRef]